INTERNATIONAL TABLES FOR CRYSTALLOGRAPHY

ISSN 1574-8707
it.iucr.org

Volume I, X-ray Absorption Spectroscopy and Related Techniques
ISBN: 978-1-119-43394-1

Chapter 3.39

Keywords: X-ray absorption spectroscopy; X-ray fluorescence; harmonic contamination; daisy wheels.

Daisy wheels and the monitoring, measurement and correction of harmonic contamination and fluorescence background

Christopher T. Chantler*

School of Physics, University of Melbourne, Parkville, Victoria 3010, Australia. *Correspondence e-mail: chantler@unimelb.edu.au

Filter banks can be used to investigate the contributions of harmonics to the beam on sample or in various multiple-sample approaches. A challenge is to make these measurements fast, efficient and automated, whether for beamline characterization or diagnosis, or for the accurate measurement of X-ray absorption spectroscopy (XAS) in either transmission or fluorescence. Similarly, complex angular-dependent measurements can quantify elastic and inelastic scattering and fluorescence. A challenge is to quantify these within experiment as a fast, efficient diagnostic and for the measurement of key systematic errors to extract attenuation coefficients, absorption coefficients or the XAS structure near an edge. The current implementations of daisy wheels provide a fast and efficient diagnostic.

1. Introduction

Filter banks often include reliable reference standards for different elements of some idealized, although often unknown, thickness. The foil filter in the beamline environment is often of significant age and may be contaminated from previous experiments. Also, these filter banks are far upstream and are not well placed to interrogate the harmonic of the beam on the sample or the beam energy bandwidth and divergence (de Jonge *et al.*, 2004; Bunker, 2024). Further, the slow motors are unable to investigate or monitor the beam on the fly, and often only a single thickness of a given elemental foil is included.

The use of adjustable paired *x*–*y* slits for the beam is common, although they are often some distance upstream of the sample and usually are not quickly or efficiently adjustable in an automated manner to characterize fluorescence or elastic scattering. It is valuable and important to have rapidly adjustable apertures both upstream and downstream to define orthogonal signatures of fluorescence and scattering on upstream and downstream detectors in transmission measurements.

The idea of a daisy wheel with very fast motor action is to measure a suitable set of thicknesses of a specific metal foil to characterize harmonic contamination quickly and efficiently (for example within 20 s on a second-generation bending-magnet beamline). This can be quite attractive. Similarly, using a suitable set of apertures to monitor the magnitude of fluorescence and elastic scattering on a similar timescale can be useful and significant. In principle, any fast motor with suitable calibrated foils and stages is suitable. An advantage of daisy wheels is that they can be positioned close to the sample stage, both upstream and downstream, and hence in most synchrotron environments, especially for XAS transmission

Related chapters

Volume I: 2.8, 3.13, 3.14, 3.36, 3.37, 3.38, 3.43, 4.2, 4.6, 4.7, 7.4

measurements but also for characterization using XAS measurements in fluorescence. The best demonstration of the significance of these effects is where they contribute dominant systematic and functional error to the measurement.

2. Harmonics

Tran, Barnea *et al.* (2003) investigated silicon attenuation and harmonics using three single-crystal 15 × 15 mm silicon wafers of well calibrated different thicknesses from 50 µm to 4 mm, within the attenuation range $0.5 < \ln(I_0/I) < 5$, where I_0 and I are the incident and the attenuated intensities, respectively. The [111] direction was nominally perpendicular to the wafer surface. The impurity levels of the wafers were insignificant. Ten measurements were carried out for each wafer at each energy. Energies were stepped through from 5 to 12 keV.

This enabled careful studies of systematic contributions, including harmonics, scattering and detector linearity, which are impossible to quantify using a single thickness (Tran, Chantler *et al.*, 2003).

The third-harmonic component of the X-ray beam was minimized both by the incident flux at the higher energy being lower and by detuning the second reflecting plane of the double-reflection silicon monochromator. Nevertheless, we found strong third-order harmonic contamination in the incident X-ray beam below 5.6 keV.

Fig. 1 shows a comparison between the measured mass attenuation coefficients $[\mu/\rho]$ for wafers of three thicknesses and that predicted by theory (Chantler, 1995). Above 5.6 keV, the three measurements are consistent to within 1% and confirm the trend from theory. Measurements were free from harmonic contamination in this higher energy range. Below 5.6 keV, the measured $[\mu/\rho]$ decreases systematically with increasing thickness (Fig. 2). Common understanding recommends using the thinnest foils in an appropriate energy range, and the 56 µm foil as the thinnest is indeed least affected by the harmonic content. However, the thinnest foil is still affected by several percent, while the thicker foils are affected by over 30%. In this X-ray energy region there is no absorption edge for silicon, and no significance for XAS nanostructure. Note, however, that the silicon thicknesses obey the Nordfors criterion for ideal thicknesses for XAS, yet these corrections are strongly energy-dependent and would affect the structure.

This is the effect of harmonic contamination in the beam. The predictions of the apparent attenuation agree very well with experimental data (Fig. 3).

These measurements were able to separate the effect of harmonics from any effects due to scattering or fluorescence. Harmonics will generally affect lower energy measurements,

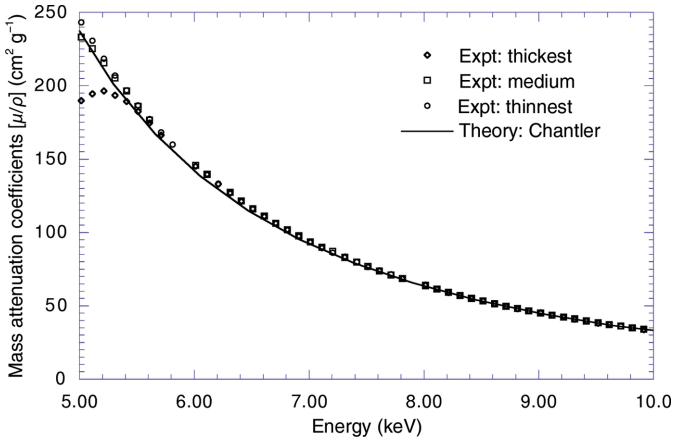

Figure 1
Results of measurements of the mass attenuation coefficient for silicon. On the scale of this graph, the measurements obtained with the three wafer thicknesses overlap at high energies. The signature of the effect of the harmonic content in the incident beam is seen below 5.6 keV (Tran, Chantler *et al.*, 2003).

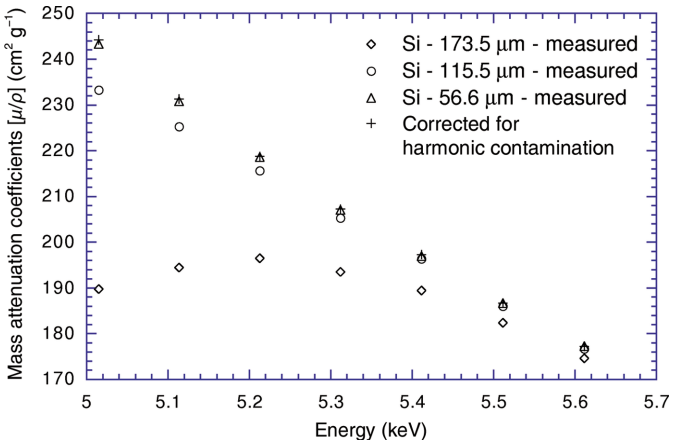

Figure 2
Effect of third-order harmonic contamination on the mass attenuation coefficients $[\mu/\rho]$ with a Si(111) monochromator and three silicon wafers. Triangles, squares and diamonds represent the measured mass attenuation coefficients corresponding to the thinnest (56.3 µm), medium (115.4 µm) and thickest (171.9 µm) silicon wafers, respectively. Crosses represent the attenuation coefficients corrected for the effect of harmonic contamination (Tran, Chantler *et al.*, 2003). Even the thinnest sample required correction for harmonics.

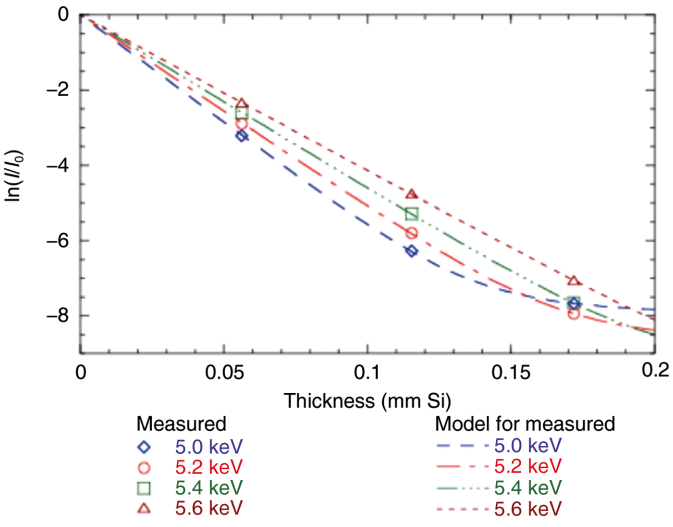

Figure 3
Summary of the modelling for the harmonic fraction at different energies using three thicknesses of silicon. The uncertainty is given by the thickness of the line.

whilst scattering will usually affect high-energy measurements, and fluorescence can dominate in different above-edge regimes. The technique of using multiple samples of accurately known thickness is quite sensitive and can reliably establish the level of harmonic contamination at 5.6 keV to within 0.01%. The final accuracy of the technique depends on the accuracy of the thickness measurements, the relative attenuation of the fundamental and harmonic radiation, and the counting statistics (Fig. 2).

This accurate thickness measurement is relatively time-consuming, and this is why daisy wheels can be very effective. It is far faster and easier to make a secondary measurement using metal daisy wheels, on the perimeter of which increasing numbers of foils are mounted that are placed in the beam by suitable rotation of the wheel (Fig. 4). This technique is accurate, reproducible and rapid, and only requires of the order of 20 s on a second-generation beamline with low flux (Tran, Barnea *et al.*, 2003).

Fig. 5 shows the measured attenuation $\ln(I/I_0)$ by 11 aluminium foils with thicknesses between 15 µm and 1 mm of X-rays doubly reflected by a monolithic silicon (111) channel-cut monochromator. Common applications have used 11–14 foils of aluminium as attenuators, with thicknesses of up to 4 mm, and a similar number of molybdenum foils for higher energies.

The experimental results follow a straight line until the thickness of aluminium increases to such an extent that the transmitted radiation consists overwhelmingly of the more energetic (15 keV) third-order harmonic. When this occurs, one observes an inflexion in the attenuation versus thickness plot, with a gradient that then approaches that of the linear attenuation coefficient of aluminium at the energy of the third-order harmonic. This inflexion in the plot provides clear evidence for the presence of a third-order harmonic [the (222) reflection of silicon is 'forbidden']. The solid curve in Fig. 5 is the thickness dependence of the attenuation of aluminium for 5 keV X-rays with an admixture of 1.09% ± 0.02% of the 15 keV third-order harmonic, as can be confirmed by extrapolating the slope in the second 'linear' portion of the graph for thicknesses above 0.2 mm back to zero thickness.

This quantitatively determines the fraction of the harmonic present in the beam and therefore can investigate the effects of tuning and detuning on the harmonic fraction, or the effects of harmonic rejection mirrors. Fig. 6 compares the effects of tuning and detuning on the harmonic fraction. Diamonds correspond to the attenuation measurements after the application of a fixed tuning current, squares correspond to the attenuation measurements with the monochromator in its natural mode with no tuning or detuning, and triangles correspond to the same measurements after the application of a fixed (large) detuning current. The dashed, dotted–dashed

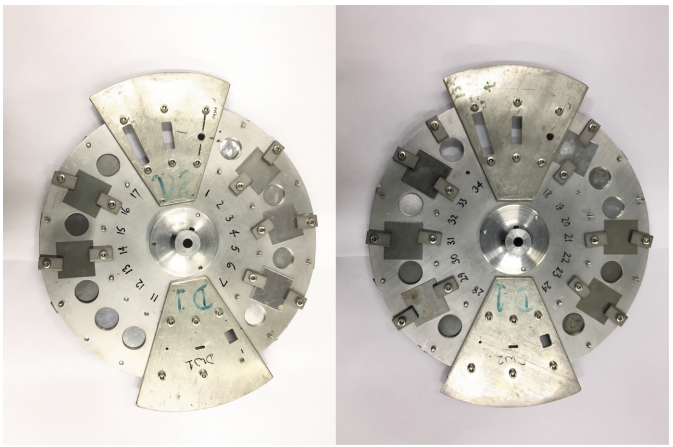

(*a*) (*b*)

Figure 4
Daisy wheels: (*a*) upstream daisy wheel and (*b*) downstream daisy wheel. Different thickness of aluminium foil and molybdenum foils are attached along the perimeter of the daisy wheel to measure the harmonic component of the X-ray beam. Different sizes of apertures on the daisy wheels are used to quantify the scattering and the fluorescence radiation of the main beam.

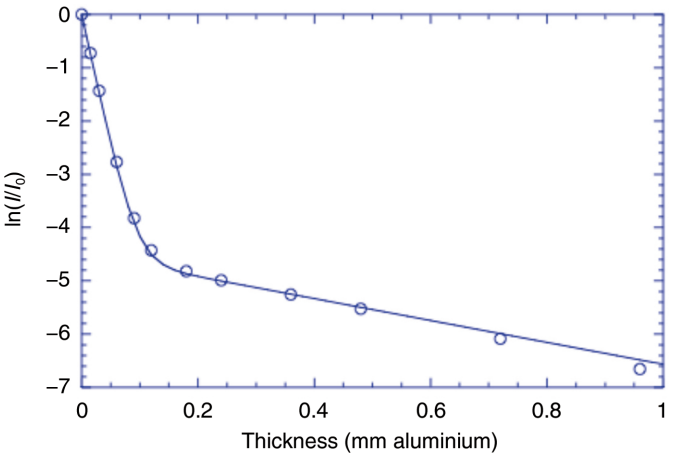

Figure 5
The attenuation, $\ln(I/I_0)$, as a function of the thickness of the aluminium absorber in a 5 keV X-ray beam. The circles are the experimental results and the solid line is the curve of best fit corresponding to an admixture of 1.09% ± 0.02% third-order harmonic (15 keV).

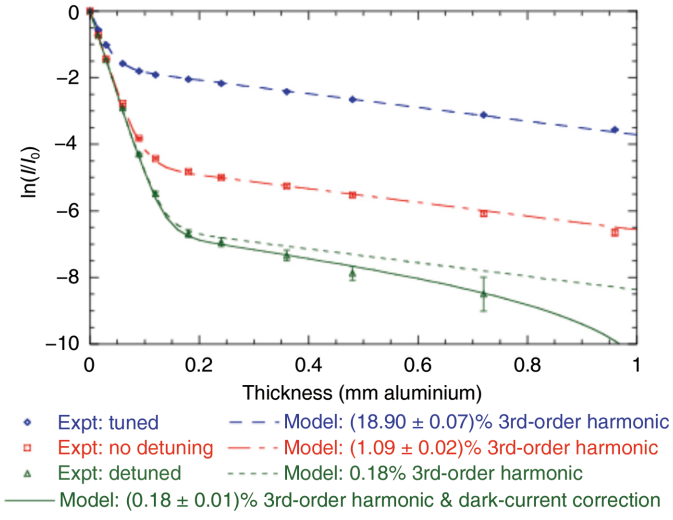

Figure 6
The effects of tuning and detuning the monochromator at a setting of 5 keV compared with the default (no) detuning.

and dotted curves are fitted curves with 18.90% ± 0.07%, 1.09% ± 0.02% and 0.18% ± 0.01% 15 keV third-order harmonic in the incident, unattenuated beam, respectively. The dotted curve demonstrates the decrease in the harmonic component that is achieved by detuning, noting that the effect remains measurable.

Similarly, investigations with daisy wheels determined the effective harmonic content in measurements around and below the Cu *K* edge (Glover *et al.*, 2008). Significant harmonic content was detected below 8 keV and is plotted in Fig. 7. This is related to the effective or apparent harmonic content, reflecting the apparent contamination; from this, the harmonic photon percentage in the incident beam can be derived (Glover & Chantler, 2009). This contamination was also clearly measured in experiments on silver (Islam *et al.*, 2014) and was investigated down to 8 keV in experiments on zinc selenide (Sier *et al.*, 2020) and down to 8 keV on zinc at a third-generation source with harmonic rejection mirrors (Ekanayake *et al.*, 2021*a*).

Abe *et al.* (2018) suggest that a generally accepted harmonic content limit for transmission XAFS is $<10^{-5}$. This is an attainable ideal, but is not generally achievable with a single reduction approach (*i.e.* with detuning or a harmonic rejection mirror). Note that tuning and detuning change the incident energy upon the sample and harmonic rejection mirrors change the bandpass, so that for high accuracy or structure the level of detuning and energy shift should be measured, perhaps following Tran *et al.* (2024). Then again, until the advent of daisy wheels this was also unable to be measured. From the figures, we can see that if the uncorrected harmonic content is, for example, 1% then we can use detuning or a harmonic rejection mirror to reduce it to, for example, 0.01%. Across this range the daisy wheels can measure this effective content to within about a percent, as seen in the figures: 0.18% ± 0.01%. Whilst other (much slower) methods exist including calibrated filter banks, calibrated reference samples as with silicon thicknesses, and wedges, the daisy-wheel approach is faster by some two orders of magnitude and just as accurate. Hence, it is reasonable to quantify effective harmonic content down towards 10^{-4} and to recommend that it be monitored and measured towards this level. Conversely, perhaps, any harmonic content below 10^{-4} is as yet not measurable.

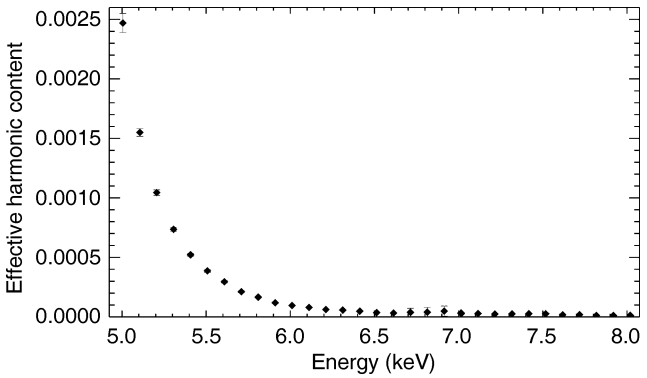

Figure 7
The effective harmonic content between 5 and 8 keV. Above 8 keV the effective harmonic content did not differ significantly from zero (Glover *et al.*, 2008).

A two-orders-of-magnitude reduction is not enough if, for example, the original effective harmonic content was 10–30%, which occurs at lower energies (Fig. 6). In this situation, combined methods, a harmonic rejection mirror and possible detuning, can be effective, and of course can be monitored by the daisy-wheel signatures. Note that in this figure the improvement compared with full tuning is indeed three orders of magnitude, changing from 18.9% to 0.18%. A second comment is that harmonic content adds to the background, especially below the edge, and strongly affects thicker sample measurement, so using 2–3 sample thicknesses can reveal the effect of this signature where a single thickness may not. If the harmonic contribution is measured and hence can be corrected for, then 0.18% or so is perfectly acceptable and indeed can be corrected for very well with multiple thicknesses.

A corollary of this is a discussion of limitations. These daisy-wheel thicknesses have been optimized for energies above 5 keV, including up to 60 keV. Significant harmonic content may well appear towards the lower range of these energies. Alternate sets of daisy wheels can be optimized for, for example, 3–5 keV. However, if the effective harmonic content becomes too large (20–70%) then the effectiveness of the diagnostic and hence of the correction becomes more limited. Further, below 5 keV the effect of the air path and windows become significant and the equivalent daisy wheels and motors should be *in vacuo*.

In other chapters (see, for example, Chantler, 2024*a*) the extended Nordfors criterion is cited, where μt = 6.0 is an acceptable total absorption for transmission XAFS. Note that this comment is related to the statistical precision and not to the influence of different systematic errors. In general, characterization of the dark current, blank and dead-time corrections can dominate and particularly affect both thick and thin, and intermediate thickness, samples. This criterion limit μt = 6.0, the thick sample regime, will naturally be much more strongly affected by harmonic content and less affected by roughness or heterogeneity in the sample or interface. If only a single thickness is measured, this condition may require a harmonic content of 10^{-4} or lower in the incident beam. However, with more than one thickness diagnosis of the effective harmonic content permits a correction which is usually accurate to 1% or better and then does not limit the XAS spectrum or structural determination.

Some decades ago, Sayers (2000) stated ‘if possible a harmonic detector should be operated throughout the data collection’. Currently, the daisy-wheel approach is the only one which has and can be used and operated throughout data collection. This is explored more fully in Chantler (2024*b*,*c*,*d*). Above 5 keV this is perfectly general, and indeed the single experimental realization can work within 10–18 s per diagnostic energy from 5 keV through 60 keV, with improved optimizations and speed if a narrower energy range is involved. Below about 5 keV, a different in-vacuum optimization is needed, but is well defined by the current protocols.

3. Scattering and fluorescence

The same daisy wheels can also include fast-switchable apertures to investigate scattering and especially fluorescence (Chantler *et al.*, 2001; Tran *et al.*, 2004). This permits the investigation and measurement of the difference between absorption coefficients and attenuation coefficients, which in principle is particularly important for comparison with theory. Scattering can be represented by Bragg–Laue peaks (Tran, Barnea *et al.*, 2003) and comparison of these with Rayleigh predictions and thermal diffuse scattering (Chantler *et al.*, 2001), or more commonly with fluorescence contributions (Tran *et al.*, 2005). Typically, between the ion chambers and the sample stage there are two daisy wheels made of 2 mm thick copper. Near the rim of each daisy wheel there are three circular apertures with diameters of, for example, 3, 6 and 16 mm. With the distance between the ion chambers and the specimen being 295 mm in this example, these apertures define cones with opening half angles of 5, 10 and 27 mrad, corresponding to solid angles of 8.1×10^{-5}, 3.2×10^{-4} and 2.3×10^{-3} steradians, respectively. Attenuation measurements were carried out with three aperture combinations or more in turn at each energy to admit different amounts of fluorescent and scattered photons into the detectors. Other aperture shapes were used in other experimental configurations, and it is important to consider symmetric and asymmetric combinations of apertures for the upstream and downstream daisy wheels impacting upon the upstream and downstream ion chambers. Compared with a small point aperture, fluorescence increases the signal from the sample isotropically to both upstream and downstream detectors, and the distance to the aperture from the sample defines the solid angle for fluorescence. The effects are often towards the 0.4–1% level (Sier *et al.*, 2020), especially above and near the edge. From Ekanayake *et al.* (2021*a*), corrections to the mass attenuation for zinc metal foils were up to 35% on the rising slope of the edge, with a maximum of 6% in the near-edge region for thin foils and 13% or 9% for the thicker foils used. After correction, the uncertainty, from the variance, is better than 0.028%, but without correction the errors with structural dependence upon energy can be 9% or more for a typical thickness or aperture (Ekanayake *et al.*, 2021*b*). A key finding of a detailed study at this third-generation source using a wiggler was the presence of background scattering of the Zn *K* edge from zinc contamination of the beamline upstream of the sample, which significantly affected the data, given the daisy-wheel aperture measurements (Sier *et al.*, 2022).

4. Conclusion

Well characterized third-generation source beamlines often use optimized detuning or harmonic rejection mirrors. This can be measured and quantified down to an effective harmonic contamination below 10^{-5}, which can be especially important towards lower beam energies. As a diagnostic, the use of daisy wheels optimized for the relevant energy range and beamline can be very fast and efficient.

For accurate measurements near the edge, where fluorescence can be strong, the use of two daisy wheels with multiple apertures upstream and downstream can correct for structural contributions above and below the edge for transmission measurements from over 15% down to a final accuracy below 0.02%. This enhances possible structural insight and the ability of theory to predict low-*k* and pre-edge structure.

References

Abe, H., Aquilanti, G., Boada, R., Bunker, B., Glatzel, P., Nachtegaal, M. & Pascarelli, S. (2018). *J. Synchrotron Rad.* **25**, 972–980.
Bunker, G. (2024). *Int. Tables Crystallogr. I*, ch. 3.45, 567–571.
Chantler, C. T. (1995). *J. Phys. Chem. Ref. Data*, **24**, 71–643.
Chantler, C. T. (2024*a*). *Int. Tables Crystallogr. I*, ch. 2.8, 88–99.
Chantler, C. T. (2024*b*). *Int. Tables Crystallogr. I*, ch. 3.38, 537–538.
Chantler, C. T. (2024*c*). *Int. Tables Crystallogr. I*, ch. 3.46, 572–573.
Chantler, C. T. (2024*d*). *Int. Tables Crystallogr. I*, ch. 3.43, 558–563.
Chantler, C. T., Tran, C. Q., Paterson, D., Barnea, Z. & Cookson, D. J. (2001). *Radiat. Phys. Chem.* **61**, 347–350.
de Jonge, M. D., Barnea, Z., Tran, C. Q. & Chantler, C. T. (2004). *Phys. Rev. A*, **69**, 022717.
Ekanayake, R. S. K., Chantler, C. T., Sier, D., Schalken, M. J., Illig, A. J., de Jonge, M. D., Johannessen, B., Kappen, P. & Tran, C. Q. (2021*a*). *J. Synchrotron Rad.* **28**, 1476–1491.
Ekanayake, R. S. K., Chantler, C. T., Sier, D., Schalken, M. J., Illig, A. J., de Jonge, M. D., Johannessen, B., Kappen, P. & Tran, C. Q. (2021*b*). *J. Synchrotron Rad.* **28**, 1492–1503.
Glover, J. L. & Chantler, C. T. (2009). *X-ray Spectrom.* **38**, 510–512.
Glover, J. L., Chantler, C. T., Barnea, Z., Rae, N. A., Tran, C. Q., Creagh, D. C., Paterson, D. & Dhal, B. B. (2008). *Phys. Rev. A*, **78**, 052902.
Islam, M. T., Tantau, L. J., Rae, N. A., Barnea, Z., Tran, C. Q. & Chantler, C. T. (2014). *J. Synchrotron Rad.* **21**, 413–423.
Sayers, D. E. (2000). *Report of the International XAFS Society Standards and Criteria Committee*. http://ixs.iit.edu/IXS/subcommittee_reports/sc/SC00report.pdf.
Sier, D., Cousland, G. P., Trevorah, R. M., Ekanayake, R. S. K., Tran, C. Q., Hester, J. R. & Chantler, C. T. (2020). *J. Synchrotron Rad.* **27**, 1262–1277.
Sier, D., Ekanayake, R. S. K. & Chantler, C. T. (2022). *X-ray Spectrom.* **51**, 91–100.
Tran, C. Q., Barnea, Z., de Jonge, M. D., Dhal, B. B., Paterson, D., Cookson, D. J. & Chantler, C. T. (2003). *X-ray Spectrom.* **32**, 69–74.
Tran, C. Q., Chantler, C. T., Barnea, Z., de Jonge, M. D., Dhal, B. B., Chung, C. T. Y., Paterson, D. & Wang, J. (2005). *J. Phys. B At. Mol. Opt. Phys.* **38**, 89–107.
Tran, C. Q., Chantler, C. T., Barnea, Z., Paterson, D. & Cookson, D. J. (2003). *Phys. Rev. A*, **67**, 042716.
Tran, C. Q., Chantler, C. T. & de Jonge, M. D. (2024). *Int. Tables Crystallogr. I*, ch. 3.42, 549–557.
Tran, C. Q., de Jonge, M., Barnea, Z. & Chantler, C. T. (2004). *J. Phys. B At. Mol. Opt. Phys.* **37**, 3163–3176.